

PAPER

## Robust transmission of orbital angular momentum mode based on a dual-cladding photonic quasi-crystal fiber

To cite this article: Exian Liu *et al* 2019 *J. Phys. D: Appl. Phys.* **52** 325110

View the [article online](#) for updates and enhancements.



**IOP | ebooks<sup>TM</sup>**

Bringing you innovative digital publishing with leading voices  
to create your essential collection of books in STEM research.

Start exploring the collection - download the first chapter of  
every title for free.

# Robust transmission of orbital angular momentum mode based on a dual-cladding photonic quasi-crystal fiber

Exian Liu, Wei Tan, Bei Yan, Jianlan Xie, Rui Ge and Jianjun Liu<sup>ID</sup>

Key Laboratory for Micro/Nano Optoelectronic Devices of Ministry of Education & Hunan Provincial Key Laboratory of Low-Dimensional Structural Physics and Devices, School of Physics and Electronics, Hunan University, Changsha 410082, People's Republic of China

E-mail: [jianjun.liu@hnu.edu.cn](mailto:jianjun.liu@hnu.edu.cn)

Received 14 February 2019, revised 14 May 2019

Accepted for publication 21 May 2019

Published 13 June 2019



## Abstract

A dual-cladding photonic quasi-crystal fiber is theoretically proposed to robustly transmit orbital angular momentum (OAM) modes. This fiber, based on conventional silica background, can lift the effective index separation of constituent vortex modes to the order of  $10^{-2}$  in the band of  $>200\text{ nm}$ , surpassing two orders of magnitude than that of common silica-based fibers. Moreover, the effective index separations in first order group ( $\text{TE}_{01}$ ,  $\text{HE}_{21}$ , and  $\text{TM}_{01}$ ) present an opposite and near-linear variation with the increase of air-filling fraction of inner and outer cladding. The mode  $\text{TE}_{01}$  can simultaneously realize an ultra-flattened dispersion with a maximum variation of  $19.736\text{ ps/nm/km}$  and low confinement loss of order of  $10^{-2}\text{ dB m}^{-1}$  within a  $400\text{ nm}$  bandwidth covering the communication bands of E, S, C, L and U. Detailed investigation on bend-induced influence shows that this fiber can remain well OAM propagation property with the bending radius being more than  $30\text{ }\mu\text{m}$ . In addition, the robustness of OAM property is also stressed with assuming  $\pm 3\%$  deviation of diameter of all air holes due to imperfect fiber preparation. This design is expected for the application of OAM optical communication system and to provide guidance for engineering the large-index-separation fiber.

Keywords: OAM mode, photonic quasi-crystal fiber, effective index separation

(Some figures may appear in colour only in the online journal)

## 1. Introduction

Photonic crystal fiber (PCF), featuring with periodic microscopic air holes along its length, currently has broad applications in quantum optics [1], high-quality amplifier [2], filter [3], sensor [4], and laser [5], etc. This originates from the well-known high-flexibility of the guiding property by controlling the structural degrees of freedom. Benefiting from this characteristic, PCF is considered as a perfect candidate for transmitting the light's orbital angular momentum (OAM), which has been inspiring immense interest due to the unique spatial helical phase front and strong naturally maintained polarization states during OAM propagation [6]. OAM-supported fiber enables various applications in fields [7] including optical tweezer,

photon entanglement, atom manipulation, optical imaging, especially optical communication in which mode division multiplexing is expected as a potential groundbreaking approach to meet the need of surging capacity crunch with exponential growth of telecommunication data [8]. The beginning research for optical communications is demonstrated in free-space experiment [9]. However, the covered transmitting distance in free-space is very short (several or hundreds meters) and is easily spoiled by inevitable atmospheric turbulence. Solving this problem, specially designed fibers like PCF have been demonstrated to efficiently generate or transmit OAM lights with more than one-kilometer propagation distance [10, 11].

Essentially, fiber that supports OAM modes must possess a large enough effective index separation  $\Delta n_{\text{eff}}$  between

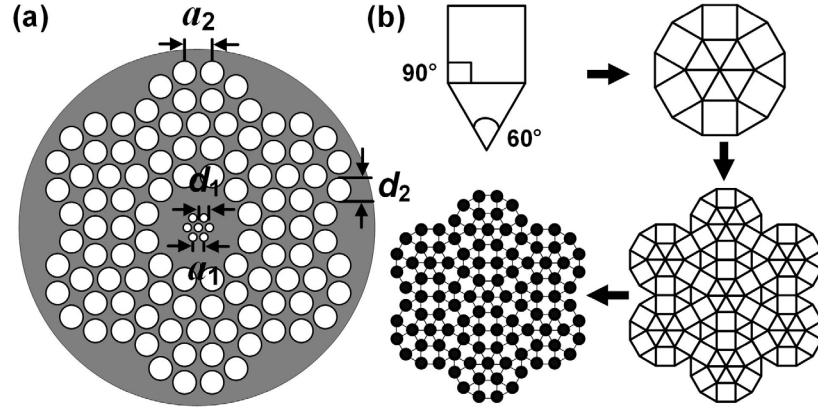


**Figure 1.** (a) Cross section of the dual-cladding Stampfli-type PQF; (b) formation process of Stampfli-type quasi-crystal lattice array.

different OAM modes (i.e. constituent HE/EH modes) to avoid the mode crosstalk. The  $\Delta n_{\text{eff}}$  generally cannot be less than the threshold of  $1.8 \times 10^{-4}$  [12]. If not, the constituent modes belonging to same mode group (e.g. all the TE<sub>01</sub>, TM<sub>01</sub> and HE<sub>21</sub> belong to LP<sub>01</sub> group) will couple between them randomly, giving rise to OAM instability problem, i.e. the formation of the undesired LP mode. In addition, too small  $\Delta n_{\text{eff}}$  will cause a short OAM propagation distance ( $< 100$  m) due to the experienced high losses [13]. In order to improve OAM mode stability and propagation distance, various fiber techniques have been proposed to lift the  $\Delta n_{\text{eff}}$  and mainly boil down to the optimization of fiber structure or material to produce a high-index ring-core in fiber.

The preferred mean is to use the conventional fiber with an embedded highly-doped ring. The index of doped material and diameter of ring-core are controllable to achieve OAM mode propagation. This kind of structure includes inverse-parabolic-index-ring fiber [13], hollow center ring-core fiber [14], dual-guided-core fiber [15] and twisted ring-core fiber [16], etc, typically realizing a  $\Delta n_{\text{eff}}$  of order of  $10^{-4}$ . However, some formed  $\Delta n_{\text{eff}}$  at  $1.55 \mu\text{m}$ , like  $1.1 \times 10^{-4}$  or  $2.1 \times 10^{-4}$  [13, 14], are so close to the threshold. In addition, the inverse-parabolic-index profile is highly complicated, requiring a precise doped process [13]. Employing PCF is another efficient way to transmit OAM mode with a large  $\Delta n_{\text{eff}}$  owing to the high index-tailored ability of PCF. A circular PCF [17] with good annular shape can lift the  $\Delta n_{\text{eff}}$  to the order of  $10^{-3}$  for order  $l = 1$ . However, the  $\Delta n_{\text{eff}}$  for high order mode is still  $10^{-4}$  and this fiber suffers from a large dispersion of  $46.38 \text{ ps/nm/km}$  for vortex mode TE<sub>01</sub>. Apart from the optimization for fiber structure mentioned above [13–17], changing the common background materials of silica as chalcogenide that has high refractive index (e.g. As<sub>2</sub>S<sub>3</sub>) can drastically lift the effective index separation to ultra-high order of  $10^{-2}$ , efficiently breaking the near-degeneracy [18, 19]. However, such fibers either support only 2 OAM modes [18] or undergo a large dispersion variation of up to  $1000 \text{ ps/nm/km}$  in the wavelength range from  $1.1$  to  $2.0 \mu\text{m}$  [19], and both of them are not suitable for optical communication because of the strong nonlinear effects. So far, fiber based on common silica has not been reported to realize a high order of  $10^{-2}$  of

$\Delta n_{\text{eff}}$  with simultaneous ultra-flattened dispersion for optical communication.

In addition, although a large body of works [12–19] have put much attention on improving the effective index separation by structure or material optimization, bend-induced influence on OAM propagation has not been involved and needs a clear verification because large index variation in radial orientation may cause a high bending loss, electric mode distribution splitting, and even OAM mode deformation.

In this paper, a silica-based dual-cladding photonic quasi-crystal fiber (DC-PQF) is used to achieve a high order of  $10^{-2}$  of  $\Delta n_{\text{eff}}$  for all supported mode groups in a wavelength band of  $> 200 \text{ nm}$ , highly supporting robust transmission of OAM modes. Photonic quasi-crystal [20] with quasi-periodic structure has been widely applied in lenses [21–26], lasers [27], prisms [28], filters [29] and fibers [30–39], etc. The employed DC-PQF possesses unique lattice arrangement characterizing with rotational symmetry rather than translational symmetry of PCF, which enables a perfect match with the annular phase shape of OAM mode. Moreover, its high optical property-tailored ability, particularly for near-zero flattened dispersion [30, 36–37], can benefit the dispersion optimization. Numerical results reveal that the achieved maximum dispersion variation and confinement loss for TE<sub>01</sub> mode are less than  $19.736 \text{ ps/nm/km}$  and  $10^{-2} \text{ dB m}^{-1}$  within a  $400 \text{ nm}$  bandwidth from  $1.35$  to  $1.75 \mu\text{m}$ , respectively. Primarily, a systematical investigation on the bend-induced influence is carried out regarding the  $\Delta n_{\text{eff}}$ , electric mode intensity and bending loss.

## 2. Model and theory

The profile of DC-PQF is illustrated as figure 1(a). The formation process of DC-PQF is shown as figure 1(b). A basic unit comprising a square and an equilateral triangle first angularly rotates six times with a step of  $60^\circ$  to form a new unit and this new unit, as a lattice point, is rotated again by the same rule for basic unit, and so on. This arrangement of the lattice array exhibits quasi-periodic features and is called Stampfli-type tiling [30]. A part of this structure is introduced into our designed fiber as shown in figure 1(a). The fiber is set with inner and outer claddings through arranging two air-filling

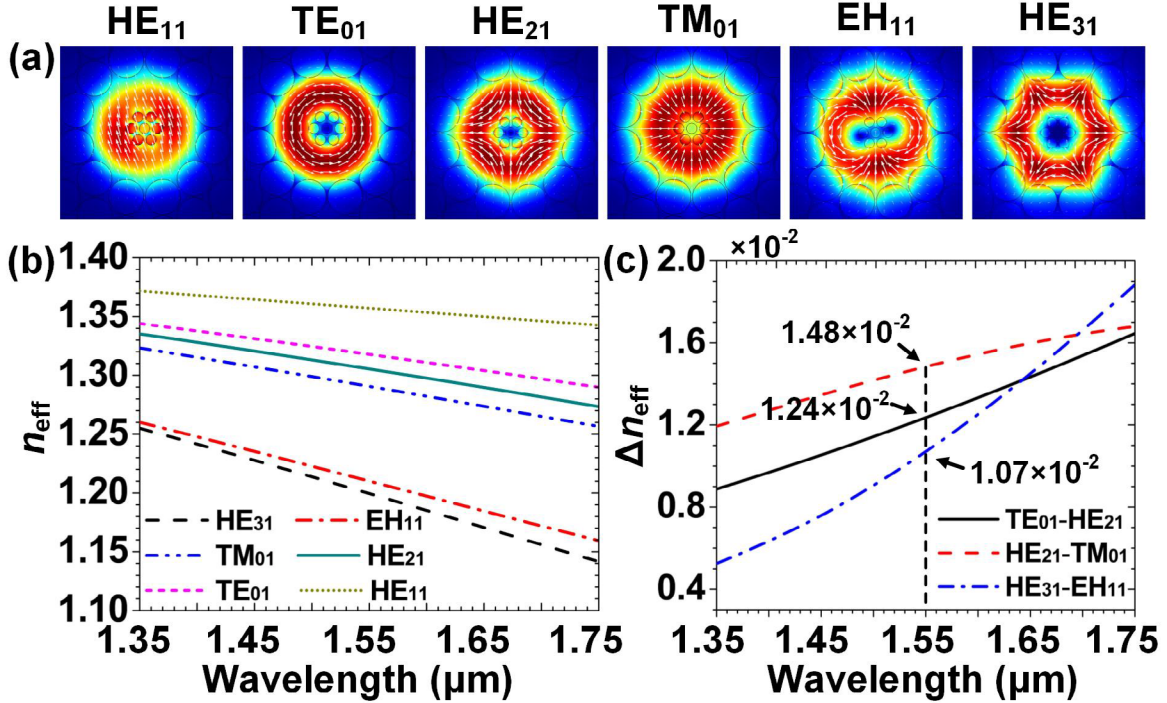


**Figure 2.** (a) Field intensities of  $\text{HE}_{11}$ ,  $\text{TE}_{01}$ ,  $\text{HE}_{21}$ ,  $\text{TM}_{01}$ ,  $\text{EH}_{11}$  and  $\text{HE}_{31}$  modes, where white arrows represent polarization states; (b) effective index  $n_{\text{eff}}$  of the supported vortex modes calculated as a function of wavelength with lattice constant  $a_1 = 0.3 \mu\text{m}$  and  $a_2 = 0.9 \mu\text{m}$ ; (c) effective index separation  $\Delta n_{\text{eff}}$  of three groups of ( $\text{TE}_{01}$ ,  $\text{HE}_{21}$ ), ( $\text{HE}_{21}$ ,  $\text{TM}_{01}$ ) and ( $\text{HE}_{31}$ ,  $\text{EH}_{11}$ ).

fractions that are the ratios of diameter of air hole to lattice constant in the inner and outer claddings. Lattice constant and diameter of air hole of the inner and outer claddings denote as  $a_1$ ,  $d_1$  and  $a_2$ ,  $d_2$  respectively. Gray background represents conventional silica with index 1.444 while white holes represent air with index 1. The DC-PQF is analyzed with the parameters of  $a_1 = 0.3 \mu\text{m}$ ,  $d_1 = 0.24 \mu\text{m}$ ,  $a_2 = 0.9 \mu\text{m}$ , and  $d_2 = 0.86 \mu\text{m}$ .

Benefiting from the dual-cladding structure, narrow guided ring-core can be constructed, which helps to separate the effective indexes of the constituent HE/EH modes and endow the fiber with a high geometric flexibility for tailoring the mode properties. By coherently combining two separated eigen even and odd HE/EH modes, OAM modes can be expressed with [16, 17]

$$\text{OAM}_{\pm l,m}^{\pm} = \text{HE}_{l+1,m}^{\text{even}} \pm j\text{HE}_{l+1,m}^{\text{odd}}, \quad (1)$$

$$\text{OAM}_{\pm l,m}^{\mp} = \text{EH}_{l-1,m}^{\text{even}} \pm j\text{EH}_{l-1,m}^{\text{odd}}, \quad (2)$$

where  $l$  denotes topological charge and  $m$  denotes the number of guided bright rings in field distribution. For  $\text{OAM}_{\pm l,m}^{\pm}$  ( $\text{OAM}_{\pm l,m}^{\mp}$ ) mode, the circular polarization has the same (opposite) direction with the field rotation [13].

For the investigation on bend-induced influence, the well-known formula  $n_b = n(x)(1 + x/R)$  [40] is adopted to calculate the refractive index  $n_b$  (at bent state) with the index  $n(x)$  (at straight state) and bending radius  $R$  (Detailed schematic diagram is illustrated in figure 7(a)). Here, the  $x$ -axis bending orientation is considered for simplicity. Therefore, the bending loss can be further deduced by utilizing the expression

$40\pi \cdot \text{Im}(n_b)/[\lambda \ln(10)]$  with the imaginary part of  $n_b$ ,  $\text{Im}(n_b)$ . For the fiber simulation at straight and bent states, COMSOL Multiphysics software based on the finite element method is utilized with a perfectly matched layer. The two-dimensional targeted region is computed with an auto triangular mesh subdivision method. The maximum mesh element size is less than  $4 \times 10^{-8} \text{ m}$  and the total number of mesh elements is 680529.

### 3. Results and discussions

#### 3.1. Effective index separation and OAM phase

We first confirm all supported vortex modes of the DC-PQF and calculate the corresponding effective indexes. The effective index separation  $\Delta n_{\text{eff}}$  between two adjacent vortex modes is primarily evaluated. The results are shown in figure 2 for the wavelength range from 1.35 to 1.75  $\mu\text{m}$ .

Figure 2(a) shows that, the DC-PQF can bear six vortex modes of  $\text{HE}_{11}$ ,  $\text{TE}_{01}$ ,  $\text{HE}_{21}$ ,  $\text{TM}_{01}$ ,  $\text{EH}_{11}$  and  $\text{HE}_{31}$  for  $m = 1$  and can provide a well confinement and well transmission quality for the guided OAM modes. This is due to the better match of intensity profile with the annular shape of DC-PQF than that of hexagonal-lattice PCF, which will help to reduce the experienced confinement loss. The effective index  $n_{\text{eff}}$  for each mode is present in figure 2(b) and all  $n_{\text{eff}}$  exhibit near-linear decrease with wavelength. Figure 2(c) shows the  $\Delta n_{\text{eff}}$  of three groups of ( $\text{TE}_{01}$ ,  $\text{HE}_{21}$ ), ( $\text{HE}_{21}$ ,  $\text{TM}_{01}$ ) and ( $\text{HE}_{31}$ ,  $\text{EH}_{11}$ ). Three  $\Delta n_{\text{eff}}$  groups increase with wavelength due to the increased mode area [18]. Crucially, the  $\Delta n_{\text{eff}}$  of both  $\text{TE}_{01}$ - $\text{HE}_{21}$  and  $\text{HE}_{21}$ - $\text{TM}_{01}$  reaches up to ultra-high order of

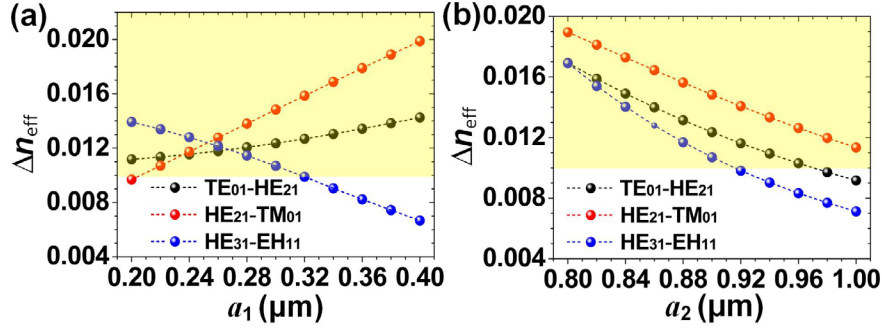


**Figure 3.** Dependence of  $\Delta n_{\text{eff}}$  on lattice constant  $a_1$  of inner cladding (a) and lattice constant  $a_2$  of outer cladding (b) at wavelength 1.55  $\mu\text{m}$ . Yellow shadow zones represent the  $\Delta n_{\text{eff}}$  that are more than the value of  $1.0 \times 10^{-2}$ .

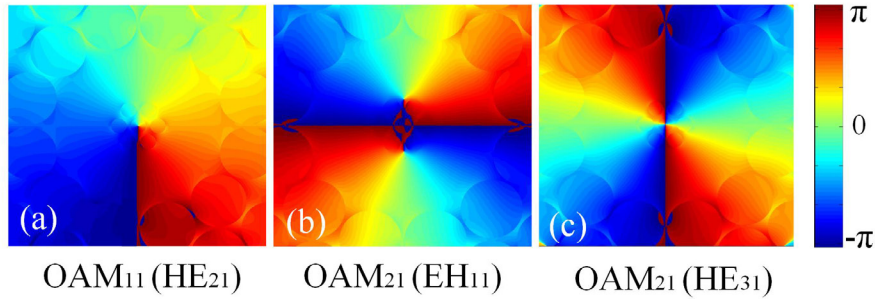


**Figure 4.** (a)–(c) Helical phase distributions of OAM<sub>11</sub> and OAM<sub>21</sub> with topological charge  $l = -1$  and  $l = -2$ . The phase (b) and (c) are achieved by combining the even and odd modes of EH<sub>11</sub> and HE<sub>31</sub>, respectively.

$10^{-2}$  in wide band of  $\sim 400$  nm (from 1.35 to 1.75  $\mu\text{m}$ ) and the  $\Delta n_{\text{eff}}$  of HE<sub>31</sub>-EH<sub>11</sub> can reach to order of  $10^{-2}$  in band of  $>200$  nm. At 1.55  $\mu\text{m}$ , the  $\Delta n_{\text{eff}}$  for three groups in the DC-PQF are  $1.48 \times 10^{-2}$ ,  $1.24 \times 10^{-2}$  and  $1.07 \times 10^{-2}$ , which are two-order-of-magnitude larger than that of most previous OAM-supported fibers [12–17, 19]. The achieved  $\Delta n_{\text{eff}}$  are the highest values for certain wavelength among all silica-based fibers [12–17], to the best of our knowledge. This can effectively ensure the stability of OAM modes when these modes transmit in the designed fiber. This can be attributed to the structure shrink (within  $\sim 1$   $\mu\text{m}$ ) and the unique configuration of PQF. To further verify the dependence of structure shrink on  $\Delta n_{\text{eff}}$ , the  $\Delta n_{\text{eff}}$  for the three groups are investigated with respect to lattice constant of inner/outer cladding while the air-filling fraction of inner/outer cladding and wavelength are fixed as 0.80/0.96 and 1.55  $\mu\text{m}$  respectively, as shown in figure 3.

Figure 3 reveals that, lattice constant has a distinct influence on improving  $\Delta n_{\text{eff}}$  and properly shrinking lattice constant can lift the  $\Delta n_{\text{eff}}$  to the order of  $10^{-2}$  for all mode groups in silica-based fiber. Therefore, the  $\Delta n_{\text{eff}}$  between constituent HE/EH modes can be largely splitted without constructing a highly-doped ring core. Furthermore, the values of DC-PQF structure parameters have same level as the chalcogenide-based OAM-supported PCF [18]. The  $\Delta n_{\text{eff}}$  of HE<sub>31</sub>-EH<sub>11</sub> gradually decreases with both lattice constant  $a_1$  and  $a_2$  increasing. However, the  $\Delta n_{\text{eff}}$  of TE<sub>01</sub>-HE<sub>21</sub> and HE<sub>21</sub>-TM<sub>01</sub> increase with  $a_1$  while decrease with  $a_2$ , which indicates  $\Delta n_{\text{eff}}$  for different groups have different sensibilities on variation of lattice constant of inner and outer claddings. Here, note that

among the supported modes of HE<sub>11</sub>, TE<sub>01</sub>, HE<sub>21</sub>, TM<sub>01</sub>, EH<sub>11</sub> and HE<sub>31</sub>, azimuthally polarized HE<sub>11</sub> and radially polarized TM<sub>01</sub> are vortex modes but not OAM modes. HE<sub>11</sub> modes with left- and right- circular polarization carrying two information-bearing states are two OAM<sub>01</sub> modes, but not strictly OAM modes.

Therefore, the DC-PQF can robustly support two OAM mode groups, OAM<sub>11</sub> and OAM<sub>21</sub>, i.e. 6 OAM modes or 8 different information bearing states including two polarization states of HE<sub>11</sub>. The phase distributions of OAM<sub>11</sub> and OAM<sub>21</sub> modes are confirmed in figures 4(a)–(c). Figures 4(a)–(c) show the helical phase distributions of OAM<sub>±1,1</sub><sup>±</sup>, OAM<sub>±2,1</sub><sup>±</sup> and OAM<sub>±2,1</sub><sup>±</sup> by inherently combining the even and odd modes of HE<sub>21</sub>, EH<sub>11</sub> and HE<sub>31</sub> respectively, according to the equations (1) and (2). All phase distributions exhibit a well phase transition from  $-\pi$  to  $\pi$ , which confirms the perfect transmission of OAM mode in the DC-PQF. For the same topological charge  $l = -2$  (figures 4(b) and (c)), the OAM phase for HE<sub>31</sub> mode shifts  $\pi/2$  angle compared with the EH<sub>11</sub> mode while they keep some circular polarization directions [16].

### 3.2. Dispersion, confinement loss, and nonlinear characteristics of OAM mode of DC-PQF

Larger  $\Delta n_{\text{eff}}$  leads to more robust OAM-mode-transmission and longer potentially transmitting distance [13]. It is also imperative to improve other optical performances with a good trade-off with large  $\Delta n_{\text{eff}}$ . Basically, flattened dispersion, low confinement loss and low nonlinear coefficient are necessary for most of fiber applications in optical communication

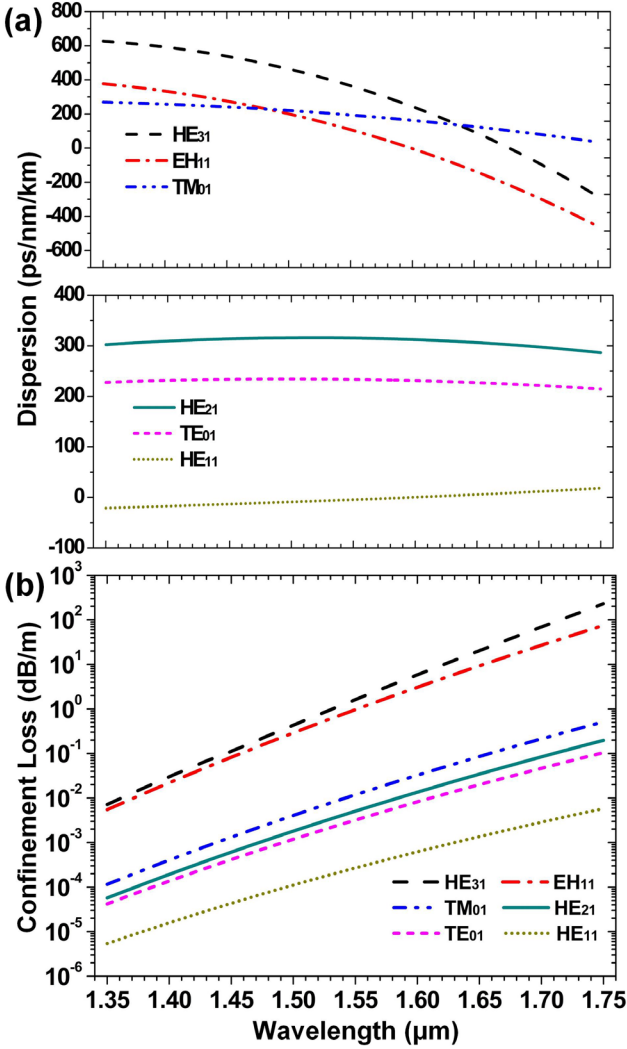


**Figure 5.** Dependence of dispersion (a) and confinement loss (b) on wavelength for all supported modes of the DC-PQF.

system. Particularly, near-zero flattened dispersion is required to maintain uniform response at different wavelengths for ultra-short pulse propagation and multiplexing communication systems. This is primary for long-distance signal propagation and super-continuum generation. Current OAM-supported fibers suffer from a large dispersion variation (up to  $\sim 200$  ps/nm/km per  $0.2 \mu\text{m}$ ) [19] or narrow low-dispersion band of less than  $0.1 \mu\text{m}$  [13, 41]. Total dispersion of the DC-PQF can be calculated by a sum of material dispersion and waveguide dispersion [30]. Material dispersion is associated with certain background material and can be calculated with Sellmeier dispersion equation [42]. The behaviors of dispersion and confinement loss of the DC-PQF are studied for all supported vortex modes in wavelength range from  $1.35$  to  $1.75 \mu\text{m}$ , as shown in figure 5.

Figure 5(a) shows that, the DC-PQF can exhibit a good dispersion behavior featuring with more flattened dispersion at lower-order mode, i.e. the dispersion is ultra-flattened for HE<sub>11</sub>, TE<sub>01</sub>, HE<sub>21</sub> and TM<sub>01</sub>. Especially for HE<sub>11</sub> mode, the dispersion can realize near-zero and ultra-flattened simultaneously. The maximum dispersion variation across

$400 \text{ nm}$  bandwidth for TE<sub>01</sub> mode is only  $19.736 \text{ ps/nm/km}$ , which is more excellent level than dispersion variation of  $\sim 60 \text{ ps/nm/km}$  [18] and hundreds of units ( $\text{ps/nm/km}$ ) [19] within approximately same bandwidth. Moreover, the involved bandwidth from  $1.35$  to  $1.75 \mu\text{m}$  covers the communication bands of E, S, C, L and U, which benefits wide-wavelength-range applications such as OAM wavelength-division multiplexing systems. In addition, we also evaluate the modal dispersion that can be qualified as the differential mode delay (DMD). DMD is related to the effective group index and the relative refractive index difference, as the [15, 43] mentioned. Our calculation suggests that the maximum and the minimum DMDs between the related OAM modes are  $32.54 \text{ ps m}^{-1}$  and  $2.10 \text{ ps m}^{-1}$ , respectively, at  $1.55 \mu\text{m}$ . This result reaches to an acceptable level compared with the values of  $18.50 \text{ ps m}^{-1}$  and  $1.10 \text{ ps m}^{-1}$  achieved in previous work [15]. Therefore, it can be concluded that the proposed DC-PQF can ensure small inter-mode nonlinear effect and present low modal dispersion.

Figure 5(b) shows the function of confinement loss as the wavelength for different supported modes, exhibiting a near-exponential increase with wavelength. This can be explained that the increased wavelength leads to decreased effective index difference between the guided ring-core mode and cladding mode to make the light more easily leak from the ring-core to the cladding, resulting in larger confinement loss. The higher the order of mode is, the larger the experienced confinement loss is for certain wavelength. At  $1.55 \mu\text{m}$ , most of the supported modes including HE<sub>11</sub>, TE<sub>01</sub>, HE<sub>21</sub> and TM<sub>01</sub> present low confinement loss, less than the order of magnitude of  $10^{-2} \text{ dB m}^{-1}$ , which exhibits similar loss property as other silica-based OAM-supported fiber [17].

Suppressing the nonlinear effects of fiber is also crucial for fiber communication to avoid signal crosstalk and signal-to-noise-ratio degradation. The measurement criterion of this effect is the value of nonlinear coefficient, which can be calculated by the expression [43]

$$\gamma(\lambda) = \frac{2\pi n_2}{\lambda A_{\text{eff}}} \quad (3)$$

where  $n_2 = 2.3 \times 10^{-20} \text{ m}^2 \text{ W}^{-1}$  is the nonlinear refractive index of the designed silica-based fiber.  $A_{\text{eff}}$  is the effective mode area that is related to electric field  $E$  distribution and can be calculated by the expression [37]

$$A_{\text{eff}} = \frac{\left( \iint |E|^2 dx dy \right)^2}{\iint |E|^4 dx dy}. \quad (4)$$

The behaviors of both nonlinearity and effective mode area are evaluated in the wavelength range from  $1.35 \mu\text{m}$  to  $1.75 \mu\text{m}$ , as shown in figure 6. Figure 6(a) shows that the nonlinear coefficients for all vortex modes gradually decrease with wavelength due to the enlarged effective mode area originated from the increased wavelength (figure 6(b)). The relationship between them is inversely proportional and nearly linear. Note that the differences of nonlinear coefficient between low-order modes are larger than that of high-order modes for certain wavelength, which is different from the near-uniform spaces achieved in PCF [17]. We attribute this to the larger effective

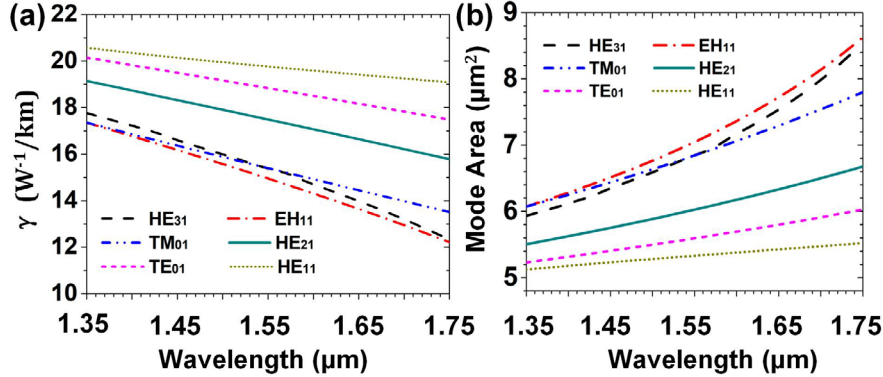


**Figure 6.** Dependence of nonlinear coefficient (a) and effective mode area (b) on wavelength for all supported modes of the DC-PQF.

index separation between low-order modes in our fiber. The higher the mode order is, the smaller the corresponding nonlinear coefficient is. The achieved values are an acceptable level compared with that of [44]. At  $1.55 \mu\text{m}$ , the nonlinear coefficient is less than  $14.95 \text{ W}^{-1} \text{ km}^{-1}$  and  $15.47 \text{ W}^{-1} \text{ km}^{-1}$  for  $\text{EH}_{11}$  and  $\text{HE}_{31}$  modes, respectively. This means that the DC-PQF can efficiently mitigate the nonlinear effects. In addition, if the background material of the DC-PQF is replaced by selenide or sulfide that has high nonlinear refractive index  $n_2$  (e.g.  $\text{As}_2\text{Se}_3$  with  $n_2$  of  $4.2 \times 10^{-18} \text{ m}^2 \text{ W}^{-1}$  or  $\text{As}_2\text{S}_3$  with  $n_2$  of  $3 \times 10^{-18} \text{ m}^2 \text{ W}^{-1}$ ), mentioned in [18, 19, 45], it is highly possible for such fiber to realize ultra-high nonlinear coefficient and large effective index separation simultaneously, which will be useful for the generation of super-continuum spectrum of different vortex modes.

### 3.3. Bend-induced influence on OAM propagation property

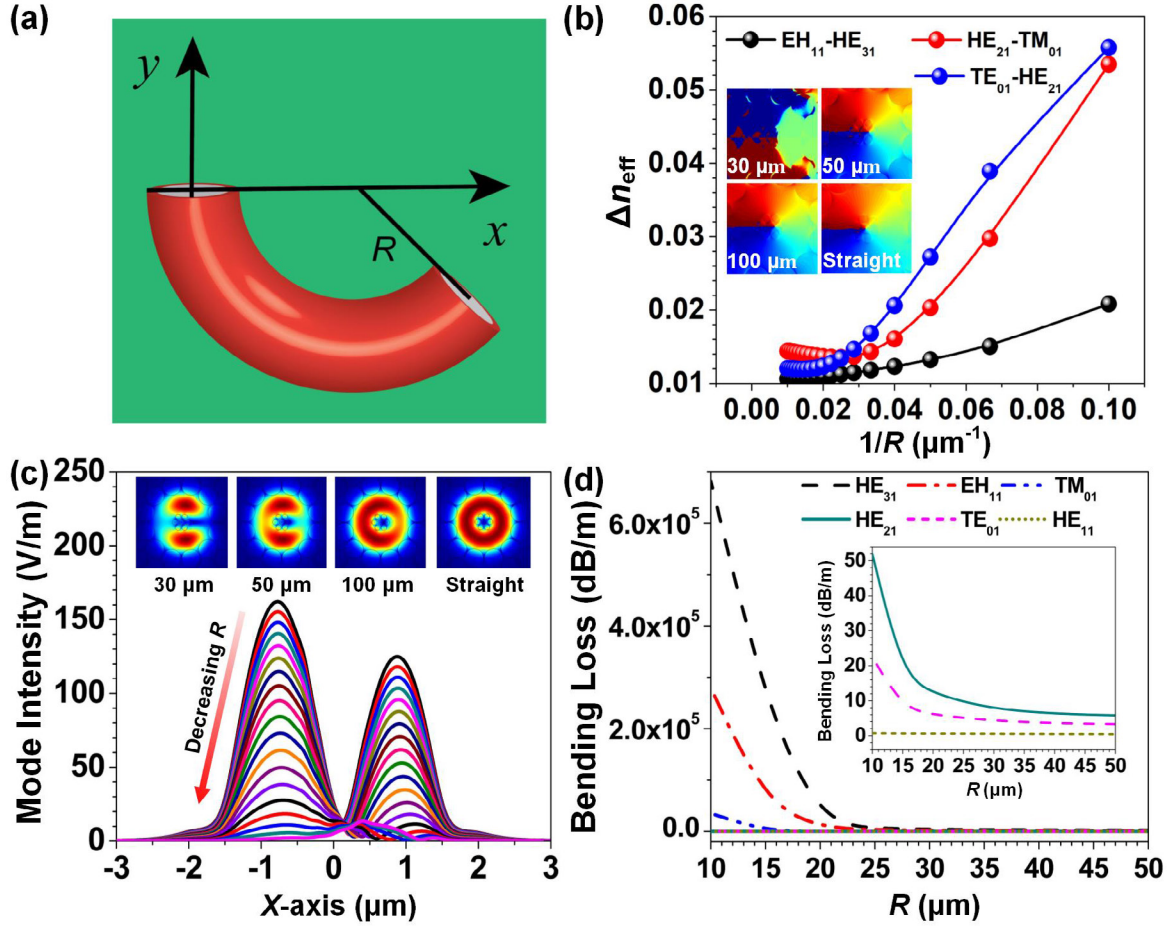
The proposed DC-PQF at straight state, discussed as the above, reveals a robust OAM transmission with well optical property. In this section, considering the bent fiber may undergo a large bending loss [46], mode field deformation [47] and highly shrunken mode area [48], the bend-induced influence on  $\Delta n_{\text{eff}}$ , electric mode intensity and bending loss is verified detailedly, as shown in figure 7.

Figure 7(a) shows the schematic diagram of the bent DC-PQF taking consideration of only  $x$ -axis orientation. Fiber bending can lead to the index change along the  $x$ -axis, damaging the mode propagation property. Figure 7(b) shows a general increasing tendency of  $\Delta n_{\text{eff}}$  with bending radius  $R$  decreasing and a steep rise occurs when  $R < 30 \mu\text{m}$  (i.e.  $1/R > 0.033 \mu\text{m}^{-1}$ ), which is associated with the mode field deformation. Note that bend-induced higher  $\Delta n_{\text{eff}}$  does not indicate the more stable OAM propagation since too small  $R$  can seriously deteriorate the OAM phase configuration. For instance, the insets in figure 7(b) show the OAM<sub>11</sub> phase profiles with  $R = 30 \mu\text{m}$ ,  $50 \mu\text{m}$ ,  $100 \mu\text{m}$  and  $+\infty$  (straight), and the OAM phase at smaller  $R$  is more deteriorated due to the increased bend-induced change in index. In fact, as bending radius  $R$  decreases, the mode field will not be a uniform angular distribution in the high-index region and eventually splitted into two parts, accompanied by the mode leakage into

cladding along  $x$ -axis orientation. It can be clearly seen by the insets in figure 7(c) in which the electric field of  $\text{TE}_{01}$  mode transfer from uniform angular distribution to two separated parts with  $R$  decreasing. However, the annular intensity distributions can remain well shape feature within high-index region benefiting from the rotational symmetric structure, which enhances the matching degree with annular shape of OAM modes. For all supported modes, the bending loss almost exponentially increase with  $R$  decreasing, showing a sharp rise when  $R$  is less than  $30 \mu\text{m}$ , as shown in figure 7(d). This increasing trend shows an agreement with inverse-parabolic graded index OAM-supported fiber [13]. For  $\text{TE}_{01}$  and  $\text{HE}_{11}$  modes, the corresponding bending loss is less than  $7.84 \text{ dB m}^{-1}$  and  $0.66 \text{ dB m}^{-1}$  respectively with  $R = 15 \mu\text{m}$ . The higher order mode suffers from larger bending loss, whose varying trend is same as that of confinement loss. That might be explained with the reduced effective refractive index difference between the ring core and cladding and relative compact fiber structure.

### 3.4. Influence of fabrication tolerance on effective index separation, dispersion and confinement loss

In addition to achieving the large effective index separation for robust OAM transmission, the robustness of the optical properties also should be emphasized since fabrication tolerance may give rise to a deterioration of property. Considering the fact that the current preparation accuracy of the diameter of air holes is within 1% [49], a simulation for the influence of fabrication tolerance on effective index separation, dispersion and confinement is carried out with assuming a larger  $\pm 3\%$  deviation of diameter of all air holes. Figures 8(a) and (b) show the variation of  $\Delta n_{\text{eff}}$  of representative  $\text{HE}_{21}$ - $\text{TM}_{01}$  and the variation of dispersion and confinement loss of  $\text{HE}_{11}$  mode, respectively. Through the comparison with original values, it can be seen that, when the diameter of air hole is increased by 3%, the  $\Delta n_{\text{eff}}$  slightly increases for each wavelength while it reduces with 3% decreasing. However, the largest variation of  $\Delta n_{\text{eff}}$  for the wavelength range is within  $2.16 \times 10^{-3}$  for the group of ( $\text{HE}_{21}$ ,  $\text{TM}_{01}$ ). At  $1.55 \mu\text{m}$ , the  $\Delta n_{\text{eff}}$  variation (or corresponding percentage) for the groups of ( $\text{TE}_{01}$ ,  $\text{HE}_{21}$ ), ( $\text{HE}_{21}$ ,  $\text{TM}_{01}$ ) and ( $\text{HE}_{31}$ ,  $\text{EH}_{11}$ ) are within  $1.0 \times 10^{-3}$  (8.1%),



**Figure 7.** (a) Schematic diagram of the bent DC-PQF; (b) dependence of  $\Delta n_{\text{eff}}$  on  $R$ ; Insets show the OAM<sub>11</sub> phase with  $R = 30 \mu\text{m}$ ,  $50 \mu\text{m}$ ,  $100 \mu\text{m}$  and  $+\infty$  (straight); (c) dependence of electric mode intensity of TE<sub>01</sub> on  $R$  in the range from  $10$  to  $100 \mu\text{m}$  with step of  $5 \mu\text{m}$ ; Insets show the mode distribution with  $R = 30 \mu\text{m}$ ,  $50 \mu\text{m}$ ,  $100 \mu\text{m}$  and  $+\infty$  (straight); (d) dependence of bending loss on  $R$  for all supported modes; inset is the magnifying figure to show the bending loss for mode HE<sub>11</sub>, TE<sub>01</sub> and HE<sub>21</sub>.

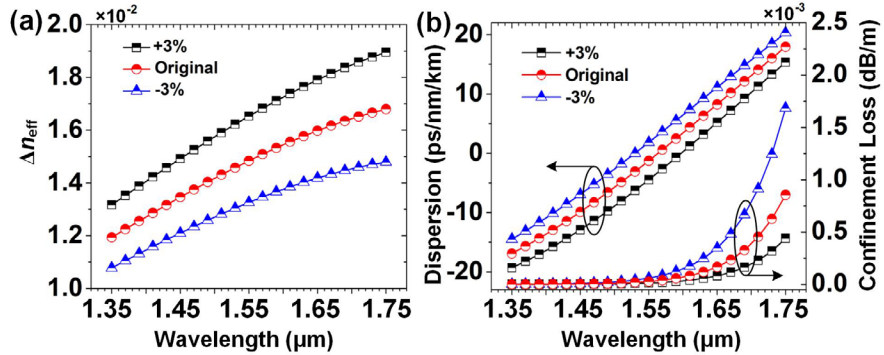


**Figure 8.** (a) Influence of  $\pm 3\%$  deviation of diameter of all air holes on the behaviors of  $\Delta n_{\text{eff}}$  of HE<sub>21</sub>-TM<sub>01</sub>; (b) dispersion and confinement loss of HE<sub>11</sub> mode.

$1.7 \times 10^{-3}$  (11.4%), and  $2.3 \times 10^{-4}$  (2.1%), respectively, with  $\pm 3\%$  deviation of air hole, which suggests that the  $\Delta n_{\text{eff}}$  can ensure a large enough value to support the OAM propagation for imperfect preparation. For the influence on dispersion and confinement loss of HE<sub>11</sub>, their deteriorations are less than  $3.2 \text{ ps/nm/km}$  and  $3.3 \times 10^{-5} \text{ dB m}^{-1}$  at wavelength  $1.55 \mu\text{m}$  and the fiber can remain near-zero flattened dispersion and low confinement loss. At longer wavelength, the influence on

confinement loss becomes more apparent, which is due to the strong wavelength-sensitive index difference between the ring core and the cladding. As discussed above, it can be deduced that the proposed DC-PQF can exhibit a good immunity to fabrication tolerance and keep a robust OAM propagation. For the practical preparation of the proposed DC-PQF, the current prevailing stack and draw technique may be not suitable to realize the quasi-periodic arrangement. The most possible

method is the sol-gel casting method, as the [50, 51] mentioned, since this method affords a wide range of design flexibility and is highly likely to achieve quasi-periodic air hole arrangement.

#### 4. Conclusions

In this paper, a silica-based DC-PQF is reported to support robust transmission of OAM modes. The achieved effective index separations of the supported vortex modes are as high as  $10^{-2}$  of the order of magnitude in bandwidth of  $>200\text{ nm}$ . It is demonstrated that properly shrinking the lattice constant could effectively enhance the effective index separation. The dependences of lattice constants of inner cladding and outer cladding on the effective index separation are different with an opposite relationship for the first order group. The DC-PQF could support 6 OAM modes or 8 different information bearing states including two  $\text{HE}_{11}$  polarization states. Furthermore, it could simultaneously realize ultra-flattened dispersion, low confinement loss and low nonlinear coefficient within a 400 nm bandwidth. Detailed investigation on bend-induced influence on the  $\Delta n_{\text{eff}}$ , electric mode intensity and bending loss is addressed and suggests that the DC-PQF can remain a well OAM propagation property with the bending radius being more than  $30\text{ }\mu\text{m}$ .

#### Acknowledgments

This work was supported by the National Natural Science Foundation of China (61405058), the Natural Science Foundation of Hunan Province (2017JJ2048), and the Fundamental Research Funds for the Central Universities (531118040112). The authors acknowledge Professor J Q Liu for software sponsorship.

#### ORCID iDs

Jianjun Liu  <https://orcid.org/0000-0002-8898-5742>

#### References

- [1] Finger M A, Iskhakov T S, Joly N Y, Chekhova M V and Russell P S J 2015 Raman-free, noble-gas-filled photonic-crystal fiber source for ultrafast, very bright twin-beam squeezed vacuum *Phys. Rev. Lett.* **115** 143602
- [2] Rosa L, Coscelli E, Poli F, Cucinotta A and Selleri S 2015 Thermal modeling of gain competition in Yb-doped large-mode-area photonic-crystal fiber amplifier *Opt. Express* **23** 18638–44
- [3] Liu Y, Chen H, Ma M, Zhang W, Wang Y and Li S 2018 Tunable ultra-broadband polarization filter based on three-core resonance of the fluid-infiltrated and gold-coated photonic crystal fiber *J. Phys. D: Appl. Phys.* **51** 125101
- [4] Liu Y, Li S, Chen H, Li J and Zhang W 2018 High-sensitivity refractive index sensor with tunable detection range based on dual-core resonance effect in gold-coated photonic crystal fibers *J. Phys. D: Appl. Phys.* **52** 055106
- [5] Wiegandt F, Anderson P N, Yu F, Treacher D J, Lloyd D T, Mosley P J, Hooker S M and Walmsley I A 2019 Quasi-phase-matched high-harmonic generation in gas-filled hollow-core photonic crystal fiber *Optica* **6** 442–7
- [6] Padgett M J 2017 Orbital angular momentum 25 years on *Opt. Express* **25** 11265–74
- [7] Yao A M and Padgett M J 2011 Orbital angular momentum: origins, behavior and applications *Adv. Opt. Photon.* **3** 161–204
- [8] Richardson D J, Fini J M and Nelson L E 2013 Space-division multiplexing in optical fibres *Nat. Photon.* **7** 354–62
- [9] Wang J *et al* 2012 Terabit free-space data transmission employing orbital angular momentum multiplexing *Nat. Photon.* **6** 488–96
- [10] Bozinovic N, Yue Y, Ren Y, Tur M, Kristensen P, Huang H, Willner A E and Ramachandran S 2013 Terabit-scale orbital angular momentum mode division multiplexing in fibers *Science* **340** 1545–8
- [11] Bozinovic N, Ramachandran S, Brodsky M and Kristensen P 2011 Record-length transmission of photons entangled in orbital angular momentum (OAM) *Frontiers in Optics, OSA Technical Digest* (San Jose, CA: Optical Society of America)
- [12] Ramachandran S, Kristensen P and Yan M F 2009 Generation and propagation of radially polarized beams in optical fibers *Opt. Lett.* **34** 2525–7
- [13] Ung B, Vaity P, Wang L, Messadeq Y, Rusch L A and LaRochelle S 2014 Few-mode fiber with inverse-parabolic graded-index profile for transmission of OAM-carrying modes *Opt. Express* **22** 18044–55
- [14] Gregg P, Kristensen P, Golowich S E, Olsen J Ø, Steinurzel P and Ramachandran S 2013 Stable transmission of 12 OAM states in air-core fiber *Proc. of CLEO CTu2K*
- [15] Zhu M, Zhang W B, Xi L X, Tang X F and Zhang X G 2015 A new designed dual-guided ring-core fiber for OAM mode transmission *Opt. Fiber Technol.* **25** 58–63
- [16] Ye J F, Li Y, Han Y Y, Deng D, Guo Z Y, Gao J M, Sun Q Q, Liu Y and Qu S L 2016 Excitation and separation of vortex modes in twisted air-core fiber *Opt. Express* **24** 8310–6
- [17] Zhang H, Zhang W B, Xi L X, Tang X F, Zhang X and Zhang X G 2016 A new type circular photonic crystal fiber for orbital angular momentum mode transmission *IEEE Photon. Technol. Lett.* **28** 1426–9
- [18] Yue Y, Zhang L, Yan Y, Ahmed N, Yang J Y, Huang H, Ren Y, Dolinar S, Tur M and Willner A E 2012 Octave-spanning supercontinuum generation of vortices in an  $\text{As}_2\text{S}_3$  ring photonic crystal fiber *Opt. Lett.* **37** 1889–91
- [19] Hu Z A, Huang Y Q, Luo A P, Cui H, Luo Z C and Xu W C 2016 Photonic crystal fiber for supporting 26 orbital angular momentum modes *Opt. Express* **24** 17285–91
- [20] Chan Y S, Chan C T and Liu Z Y 1998 Photonic band gaps in two dimensional photonic quasicrystals *Phys. Rev. Lett.* **80** 956–9
- [21] Feng Z F, Zhang X D, Wang Y Q, Li Z Y, Cheng B Y and Zhang D Z 2005 Negative refraction and imaging using 12-fold-symmetry quasicrystals *Phys. Rev. Lett.* **94** 247402
- [22] Liu J J, Liu E X, Fan Z G and Zhang X 2015 Dielectric refractive index dependence of the focusing properties of a dielectric-cylinder-type decagonal photonic quasicrystal flat lens and its photon localization *Appl. Phys. Express* **8** 112003
- [23] Liu J J, Liu E X, Zhang T H and Fan Z G 2015 Thickness dependence of two-dimensional photonic quasicrystal lens imaging characteristics *Solid State Commun.* **201** 68–71
- [24] Liu J J, Liu E X and Fan Z G 2016 Width dependence of two-dimensional photonic quasicrystal flat lens imaging characteristics *J. Mod. Opt.* **63** 692–6
- [25] Liu J J and Fan Z G 2018 Size limits for focusing of two-dimensional photonic quasicrystal lenses *IEEE Photon. Technol. Lett.* **30** 1001–4

- [26] Feng B, Liu E X, Wang Z M, Cai W C, Liu H F, Wang S, Liang T Y, Xiao W and Liu J J 2016 Generation of terahertz hollow beams by a photonic quasi-crystal flat lens *Appl. Phys. Express* **9** 062003
- [27] Vitiello M S, Nobile M, Ronzani A, Tredicucci A, Castellano F, Talora V, Li L, Linfield E H and Davies A G 2014 Photonic quasi-crystal terahertz lasers *Nat. Commun.* **5** 5884
- [28] Liu J J, Tan W, Liu E X, Hu H L, Fan Z G, Zhang T H and Zhang X 2016 Planar scanning method for detecting refraction characteristics of two-dimensional photonic quasi-crystal wedge-shaped prisms *J. Opt. Soc. Am. A* **33** 978–83
- [29] Zhao Y F, Wang Z M, Jiang Z J, Chen X, Yue C X, Wang J Z and Liu J J 2017 Add-drop filter with compound structures of photonic crystal and photonic quasicrystal *J. Infrared Millim. Waves* **36** 342–8
- [30] Kim S, Kee C S and Lee J 2007 Novel optical properties of six-fold symmetric photonic quasicrystal fibers *Opt. Express* **15** 13221–6
- [31] Cai W C, Liu E X, Feng B, Xiao W, Liu H F, Wang Z M, Wang S, Liang T Y, Liu J Q and Liu J J 2016 Dodecagonal photonic quasi-crystal fiber with high birefringence *J. Opt. Soc. Am. A* **33** 2108–14
- [32] Liu H F, Xiao W, Cai W C, Liu E X, Feng B, Wang Z M, Liang T Y, Wang S and Liu J J 2016 Photonic quasi-crystal fiber with high birefringence *Opt. Eng.* **55** 036101
- [33] Su W, Lou S Q, Zou H and Han B L 2014 Design of a highly nonlinear twin bow-tie polymer photonic quasi-crystal fiber with high birefringence *Infrared Phys. Technol.* **63** 62–8
- [34] Sivabalan S and Raina J P 2011 High normal dispersion and large mode area photonic quasi-crystal fiber stretcher *IEEE Photon. Technol. Lett.* **23** 1139–41
- [35] Su W, Lou S Q, Zou H and Han B L 2014 A highly nonlinear photonic quasi-crystal fiber with low confinement loss and flattened dispersion *Opt. Fiber Technol.* **20** 473–7
- [36] Cai W C, Liu E X, Feng B, Liu H F, Wang Z M, Xiao W, Liang T Y, Wang S and Liu J J 2016 Dispersion properties of a photonic quasi-crystal fiber with double cladding air holes *Optik* **127** 4438–42
- [37] Liu E X, Tan W, Yan B, Xie J L, Ge R and Liu J J 2018 Broadband ultra-flattened dispersion, ultra-low confinement loss and large effective mode area in an octagonal photonic quasi-crystal fiber *J. Opt. Soc. Am. A* **35** 431–6
- [38] Liu E X, Yan B, Tan W, Xie J L, Ge R and Liu J J 2018 Guiding characteristics of sunflower-type fiber *Superlattices Microstruct.* **115** 123–9
- [39] Yan B, Wang A R, Liu E X, Tan W, Xie J L, Ge R and Liu J J 2018 Polarization filtering in the visible wavelength range using surface plasmon resonance and a sunflower-type photonic quasi-crystal fiber *J. Phys. D: Appl. Phys.* **51** 155105
- [40] Wang X, Lou S Q and Lu W L 2014 Rectangle lattice large mode area photonic crystal fiber for 2 m compact high-power fiber lasers *IEEE J. Sel. Top. Quantum Electron.* **20** 200–5
- [41] Brunet C, Vaity P, Messadeq Y, LaRochelle S and Rusch L A 2014 Design, fabrication and validation of an OAM fiber supporting 36 states *Opt. Express* **22** 26117–27
- [42] Tatian B 1984 Fitting refractive-index data with the Sellmeier dispersion formula *Appl. Opt.* **23** 4477–85
- [43] Agrawal G P 2007 *Nonlinear Fiber Optics* (New York: Academic)
- [44] Zhang H, Zhang W B, Xi L X, Tang X F, Tian W, Zhang X and Zhang X G 2015 Design of a circular photonic crystal fiber supporting OAM modes *Asia Communications and Photonics Conf.*
- [45] Zhao T T, Lou S Q, Su W and Wang X 2016 Design of an As<sub>2</sub>Se<sub>3</sub>-based photonic quasi-crystal fiber with highly nonlinear and dual zero-dispersion wavelengths *J. Mod. Opt.* **63** 139–45
- [46] Matsui T, Sakamoto T, Tsujikawa K, Tomita S and Tsubokawa M 2011 Single-mode photonic crystal fiber design with ultralarge effective area and low bending loss for ultrahigh-speed WDM transmission *J. Lightwave Technol.* **29** 511–5
- [47] Saini T S, Kumar A and Sinha R K 2014 Triangular-core large-mode-area photonic crystal fiber with low bending loss for high power applications *Appl. Opt.* **53** 7246–51
- [48] Muduli N and Padhy H K 2016 An optimized configuration of large mode field area PMMA photonic crystal fiber with low bending loss: a new approach *J. Mater. Sci.* **27** 1906–12
- [49] Lou S, Tang Z and Wang L 2011 Design and optimization of broadband and polarization-insensitive dual-core photonic crystal fiber coupler *Appl. Opt.* **50** 2016–23
- [50] Kim S and Kee C S 2009 Dispersion properties of dual-core photonic quasicrystal fiber *Opt. Express* **17** 15885–90
- [51] Bise R T and Trevor D J 2005 Solgel-derived microstructured fibers: fabrication and characterization *Optical Fiber Communication Conf.* vol 3 pp 1–3